

# Langmuir probe electronics upgrade on the tokamak à configuration variable

Cite as: Rev. Sci. Instrum. **90**, 083502 (2019); <https://doi.org/10.1063/1.5108876>

Submitted: 03 May 2019 . Accepted: 23 July 2019 . Published Online: 13 August 2019

H. De Oliveira , P. Marmillod , C. Theiler , R. Chavan , O. Février , B. Labit, P. Lavanchy, B. Marlétaz, R. A. Pitts , and TCV team



View Online



Export Citation



CrossMark

## ARTICLES YOU MAY BE INTERESTED IN

[Analysis of wall-embedded Langmuir probe signals in different conditions on the Tokamak à Configuration Variable](#)

Review of Scientific Instruments **89**, 053502 (2018); <https://doi.org/10.1063/1.5022459>

[Ultra-high-bandwidth polarization interferometry and optimal quadratic phase detection](#)

Review of Scientific Instruments **90**, 083503 (2019); <https://doi.org/10.1063/1.5091569>

[The digital mirror Langmuir probe: Field programmable gate array implementation of real-time Langmuir probe biasing](#)

Review of Scientific Instruments **90**, 083504 (2019); <https://doi.org/10.1063/1.5109834>



Lock-in Amplifiers

Zurich Instruments

Watch the Video

# Langmuir probe electronics upgrade on the tokamak à configuration variable

Cite as: Rev. Sci. Instrum. 90, 083502 (2019); doi: 10.1063/1.5108876

Submitted: 3 May 2019 • Accepted: 23 July 2019 •

Published Online: 13 August 2019



View Online



Export Citation



CrossMark

H. De Oliveira,<sup>1,a)</sup> P. Marmillod,<sup>1</sup> C. Theiler,<sup>1</sup> R. Chavan,<sup>1</sup> O. Février,<sup>1</sup> B. Labit,<sup>1</sup> P. Lavanchy,<sup>1</sup> B. Marlétaz,<sup>1</sup> R. A. Pitts,<sup>2</sup> and TCV team<sup>b)</sup>

## AFFILIATIONS

<sup>1</sup>Ecole Polytechnique Fédérale de Lausanne (EPFL), Swiss Plasma Center (SPC), CH-1015 Lausanne, Switzerland

<sup>2</sup>ITER Organization, Route de Vinon sur Verdon, CS90 046, 13067 St Paul Lez Durance, Cedex, France

<sup>a)</sup>[hugo.deoliveira@epfl.ch](mailto:hugo.deoliveira@epfl.ch)

<sup>b)</sup>See author list of S. Coda *et al.*, Nucl. Fusion **57**, 102011 (2017).

## ABSTRACT

A detailed description of the Langmuir probe electronics upgrade for TCV (*Tokamak à Configuration Variable*) is presented. The number of amplifiers and corresponding electronics has been increased from 48 to 120 in order to simultaneously connect all of the 114 Langmuir probes currently mounted in the TCV divertor and main-wall tiles. Another set of 108 amplifiers is ready to be installed in order to connect 80 new probes, built in the frame of the TCV divertor upgrade. Technical details of the amplifier circuitry are discussed as well as improvements over the first generation of amplifiers developed at SPC (formerly CRPP) in 1993/1994 and over the second generation developed in 2012/2013. While the new amplifiers have been operated successfully for over a year, it was found that their silicon power transistors can be damaged during some off-normal plasma events. Possible solutions are discussed.

© 2019 Author(s). All article content, except where otherwise noted, is licensed under a Creative Commons Attribution (CC BY) license (<http://creativecommons.org/licenses/by/4.0/>). <https://doi.org/10.1063/1.5108876>

## I. INTRODUCTION

An extensive array of diagnostics is installed on TCV<sup>1,2</sup> (*Tokamak à Configuration Variable*), in order to give the most complete and accurate description possible of the plasma. Among the edge diagnostics, Langmuir probes (LP) are one of the most common tools to describe local properties in the boundary region of the plasma.<sup>3–5</sup> They typically provide measurements of ion saturation current  $I_{sat}$ , electron density  $n_e$ , electron temperature  $T_e$ , floating potential  $V_{fl}$ , and plasma potential  $V_{pl}$ . In the single probe arrangement (local measurement of the plasma properties),  $I_{sat}$ ,  $V_{fl}$ , and ion Mach number  $M$  can be readily measured with high time response, e.g., 200 kHz or higher. On the contrary,  $T_e$ ,  $V_{pl}$ , and  $n_e$  are usually obtained by relatively slow sweeping of the probe voltage, resulting in a time response of typically 1 kHz or lower. A detailed description of the analysis and interpretation of LPs in different experimental conditions on TCV has recently been presented elsewhere for wall-embedded probes<sup>6</sup> and for the pins of a fast-reciprocating probe.<sup>7</sup>

The main purpose of this paper is to present a newly developed amplifier circuitry to operate single LPs on TCV with an arbitrary bias-waveform or in floating potential mode. Compared to the first generation of custom-built amplifiers on TCV, the new circuitry features an improved amplification final stage with simpler and cheaper components, an improved current measurement, and a custom current limitation system based on suspended OP-amps. 180 of these third generation amplifiers have been built and tested, extending the total number of amplifiers from 48 to 228 units. This upgrade allows the simultaneous operation of all 114 wall-embedded single LPs currently installed on TCV,<sup>6</sup> as shown in Fig. 1, and thus substantially improves the operational flexibility. The upgrade also provides the spare amplifiers necessary to extend the wall LP array in view of the upcoming TCV divertor upgrade.<sup>8,9</sup>

This paper is organized as follows. A short description of the TCV wall-embedded LP design and the transmission lines connecting them to the amplifiers is presented in Sec. II. The design of the new amplifier circuitry is presented in detail in Sec. III, discussing, in particular, the amplification, the current limitation, and the

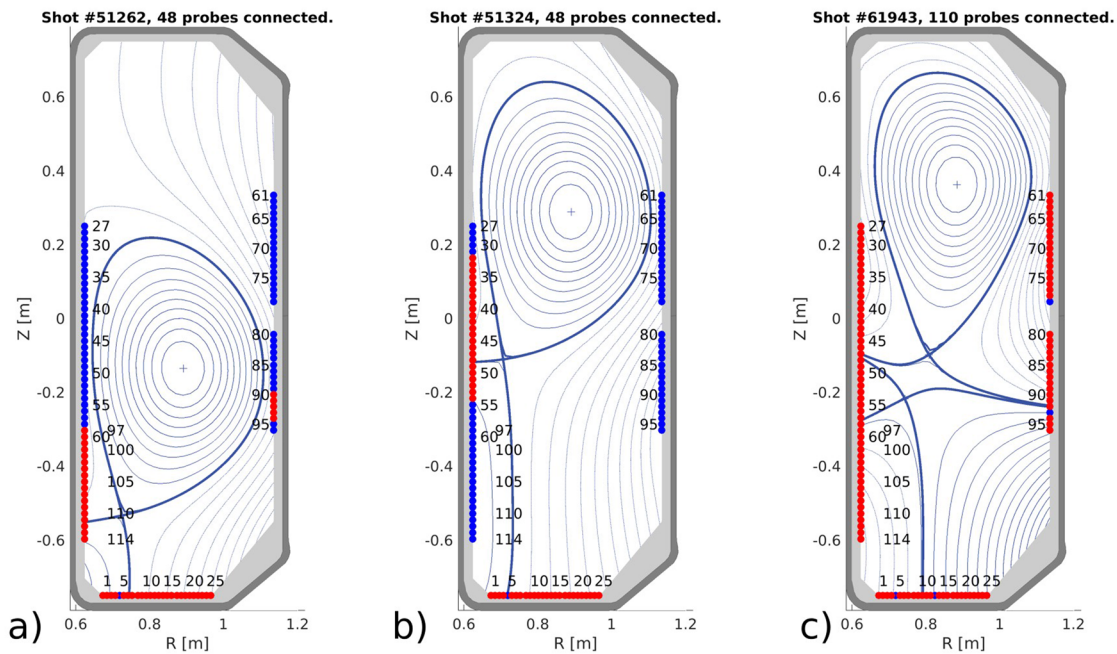


**FIG. 1.** Poloidal cross section of TCV with the location of the 114 Langmuir probe tips (red and blue dots). Before the electronics upgrade, the amplifiers needed to be rewired manually to accommodate the different plasma shapes and positions as shown in (a) for shot #51262 and in (b) for shot #51324. After the electronics upgrade, e.g., in (c), shot #61943, full coverage is attained.

voltage and current measurement circuit. Protection strategies against amplifier damage are discussed in Sec. IV, followed by a description of the TCV probe coverage planned for the TCV upgrade in baffled and nonbaffled configurations in Sec. V. Finally, a summary of the paper is presented in Sec. VI.

## II. DESIGN OF THE LANGMUIR PROBES AND CHARACTERISTICS OF THE TRANSMISSION LINE

Langmuir probes have been present in TCV since 1992.<sup>10</sup> Those are different from the first versions, and only the most recent design is presented in this paper. Details of the spatial location of installed probes have been given in 2003,<sup>11</sup> and the different probe tip geometries used in TCV have been described recently.<sup>6</sup>

The probe assembly is housed in the TCV polycrystalline graphite tiles which armor the main wall and the divertor, as shown in Fig. 2. Electrical contact is provided by nickel based alloy springs ( $R \approx 1 \Omega$ ) positioned between the inner conductor of the mineral insulated coaxial cable 1 Zs Ac 10 from the company Thermocoax®, and the probe tips are manufactured in polycrystalline graphite SGL® Sigratine R6650. The springs were used to be made out of copper beryllium alloy with high electrical conductivity ( $R \approx 0.1 \Omega$ ) and were later discarded: some springs lost their shape because of the annealing process happening at high temperatures. The measured electrical resistance of the assembly ( $R \approx 0.5 \Omega$ ) is often lower than the resistance of the nickel based alloy springs because the current can find a direct path from the stainless steel housing (4) in Fig. 2 to the copper beryllium finger electrical contact (3) in Fig. 2.

If the current goes through the nickel based alloy spring, the electrical resistance of the assembly is  $\approx 1.4 \Omega$ . Adding copper springs in parallel with the nickel based alloy springs and electrodeposition of copper on top of the nickel based alloy springs are possible solutions considered for future installations in order to reduce the electrical resistance of this component. The mechanical link between the probe tips and the assembly is assured by the same spring.

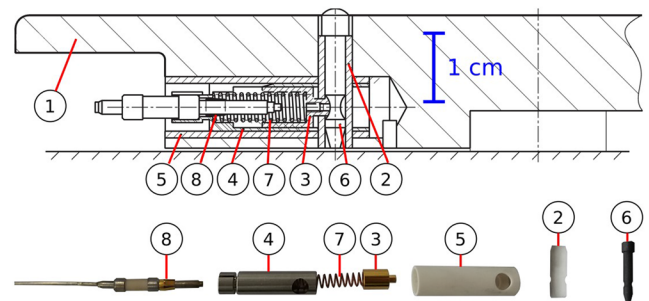


**FIG. 2.** Cross-sectional view of the probe assembly and photos of the individual components labeled as follows: ① graphite tile housing, ② vertical aluminum nitride electrical insulation tube, ③ gold coated copper beryllium finger electrical contact, ④ stainless steel housing for the cable inner conductor (end of the Thermocoax cable), ⑤ horizontal aluminum nitride electrical insulation tube, ⑥ graphite probe tip, ⑦ nickel based alloy spring, and ⑧ gold coated copper beryllium contactor (tiny ring mounted onto the cable inner conductor).

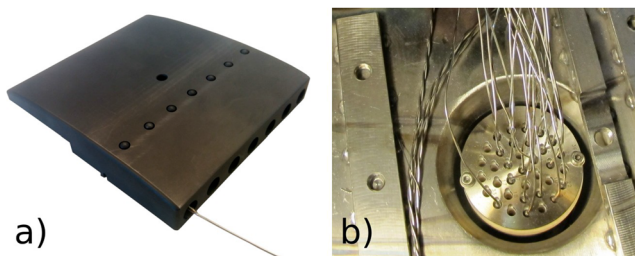


**FIG. 3.** Langmuir probe tile (a) ready for installation with a single Thermocoax cable connected to the first probe for illustration and a vacuum feedthrough (b) seen from inside the tokamak vessel after the protective tiles have been removed.

Probe tip maintenance requires the tiles to be unfastened and taken out of the machine, as illustrated in Fig. 3(a). The ease of replacement, thanks to the spring assembly, is important to minimize the down-time during manned entries in TCV. Langmuir probe tips need to be replaced when the erosion is large enough to reduce their projected area along the magnetic field. Furthermore, it was observed during the 2019 opening that a resistive layer has been deposited on most probe tip surfaces. The contact resistance measured with round-shaped electrodes is high ( $R_{\text{contact}} \approx 100 \Omega$ ) when the voltage applied is within  $\pm 1.7 \text{ V}$  and then suddenly drops ( $R_{\text{contact}} \approx 0.6 \Omega$ ) once the applied voltage is larger than  $\pm 1.7 \text{ V}$ , showing variable resistance behavior. It is difficult to evaluate the effective resistance as seen by the plasma, probably an order of magnitude lower than the measured contact resistance because of the larger contact area wetted by the plasma. Such resistive layers can affect the evaluation of the electron temperature,<sup>6</sup> particularly in the case of low electron temperature, where the most important part of the IV curve is found in a limited voltage range. It is believed that both carbon redeposition and boronization play a role in their formation. The resistive layer is supposedly very thin since a gentle sanding with a scouring pad enabled to recover both proper electrical conductance and dull appearance. High heat flux from the plasma can have the same effect as sanding: eroded probes frequently found in the near scrape-off-layer have the characteristic dull appearance from pure graphite and show negligible contact resistance.

Specific care is required when making the Thermocoax cable termination in order to ensure ultra-high vacuum (UHV) compatibility and proper electrical connection. The magnesium oxide ceramic powder electrical insulation in the Thermocoax cable acts as a moisture reservoir, and therefore, the cables must be oven dried before the connectors are brazed to seal the cable terminations. Moisture is problematic because the magnesium oxide powder becomes slightly conductive when exposed to the ambient humidity level. The electrical insulation must be tested with  $+250 \text{ V DC}$  voltage to verify if the resistance across the inner conductor and the shield of the cable is sufficiently high, i.e., at least  $100 \text{ M}\Omega$ .

The length of the Thermocoax cables between probe tips and vacuum feedthroughs, see Fig. 3(b), is typically  $\approx 2 \text{ m}$ . The vacuum feedthroughs are special units from the Kurt J. Lesker Company<sup>®</sup>. They are mounted on DN63 CF vacuum flanges. Each unit carries a maximum of 35 conductors. Electrical contact is provided by male pins embedded into the ceramic body of the feedthroughs and

by specific female copper contactors that are brazed onto the inner conductor of the Thermocoax cables.

The in-vessel transmission line is then followed with  $\approx 20 \text{ m}$  of 19 twisted pair Mueller<sup>®</sup> cables, connecting the vacuum feedthroughs with the Langmuir probe electronics cubicle. Each probe conductor from the vacuum feedthrough is connected to both conductors of each twisted pair in the Mueller cable in order to minimize the line resistance. The advantage of twisted pairs is lost by using both conductors to carry the same signal, but the high frequency properties are maintained, thanks to the individual grounded screens wrapped around each pair. Each of the 19 pair Mueller cables carries a maximum of 19 signals.

The overall capacitances of the transmission lines have been measured directly at 10 kHz and 100 kHz, and the values are found between  $C_{\text{line}} = 3.5 \text{ nF}$  and  $C_{\text{line}} = 6 \text{ nF}$  depending on the line. These measurements are consistent with measurements on spare Thermocoax cables  $C_{\text{Thermocoax}} = 0.61 \text{ nF m}^{-1}$  and on twisted pairs from spare Mueller cables  $C_{\text{Mueller}} = 0.19 \text{ nF m}^{-1}$ .

The overall resistances and inductances of the entire lines have not been measured directly. Estimates are given here based on measurements done on spare cables:

- The overall resistance is estimated to be  $R_{\text{line}} \approx 1.3 \Omega$ , given the measured DC resistance  $\approx 0.5 \Omega$  of the probe assembly shown in Fig. 2 connected to a 2 m long Thermocoax cable and given the measured resistance per unit length of a twisted pair from the Mueller cable  $R_{\text{Mueller}} \approx 0.04 \Omega \text{ m}^{-1}$ . In the scenario where nickel based alloy springs are taken into account as explained earlier, the overall resistance is estimated to be  $R_{\text{line}} \approx 2.2 \Omega$ .
- The overall inductance of the line is estimated to be  $L_{\text{line}} \approx 15.4 \mu\text{H}$ , given the measured inductance per unit length of the Thermocoax cable  $L_{\text{Thermocoax}} = 0.7 \mu\text{H m}^{-1}$  and the measured inductance per unit length of a twisted pair from the Mueller cable  $L_{\text{Mueller}} \approx 0.7 \mu\text{H m}^{-1}$  (measurements performed at 100 kHz).

Langmuir probe electronics are necessarily referenced to the vacuum vessel ground, as opposed to most diagnostics at TCV which are referenced to the TCV building ground. The electronics cubicles

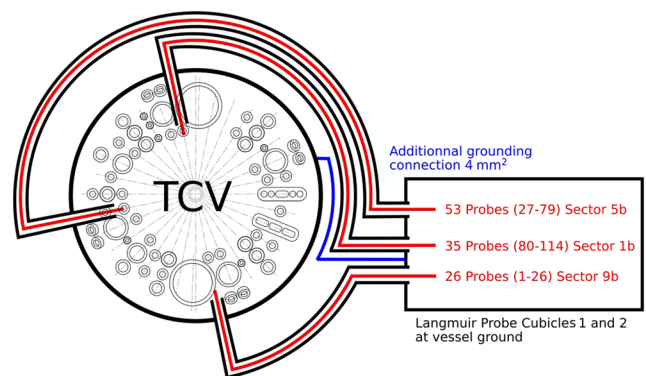


**FIG. 4.** Electrical connections in between the tokamak and the electronics cubicle with biased conductors in red and grounded conductors in black (top view).

are therefore separated from the building ground using an isolation transformer.

The 19 pair Mueller cable shield connects the electronics cubicles to the vacuum vessel ground, as sketched in Fig. 4. The cables do not encircle the vacuum vessel to avoid receiving the loop voltage induced by the central solenoid.

During a discharge, the time derivative of the vertical magnetic field can be as high as  $\approx 0.05$  T/s in the region between the vacuum vessel and the cubicles ( $r \approx 2$  m,  $z \approx -1.5$  m) mainly due to the contribution of poloidal field coils. The inductive current going through the shield can be estimated from the resistance  $R_{shield} \approx 0.1 \Omega$ . The stray current can be approximated with the laws of Ohm and Faraday,

$$I = \frac{U}{R_{shield}} = \frac{S \frac{dB}{dt}}{R_{shield}} \approx \frac{10 \text{ m}^2 \cdot 0.05 \text{ T/s}}{0.1 \Omega} \approx 5 \text{ A}. \quad (1)$$

This relatively modest stray current is not expected to perturb the measurements or the TCV magnetic field.

### III. DESIGN OF THE AMPLIFIER CIRCUITRY

There have been three different generations of Langmuir probe amplifiers developed at SPC. Only the third generation is described in detail in this paper. The first generation did not have any custom amplification module and was based on PB58A APEX® amplifiers. In the second generation, the APEX amplifier was replaced by a patch developed at SPC. The patch will not be described in this paper because it can be considered as obsolete when compared to the last generation. Indeed, the third generation features an improved current measurement and an improved current limitation system over the second generation.

This section is organized in five subsections. Section III A presents the general constraints given from plasma parameters, while Secs. III B–III E cover, respectively, the choice of power supplies, the amplification system, the potential and current measurement system, and the current limitation system.

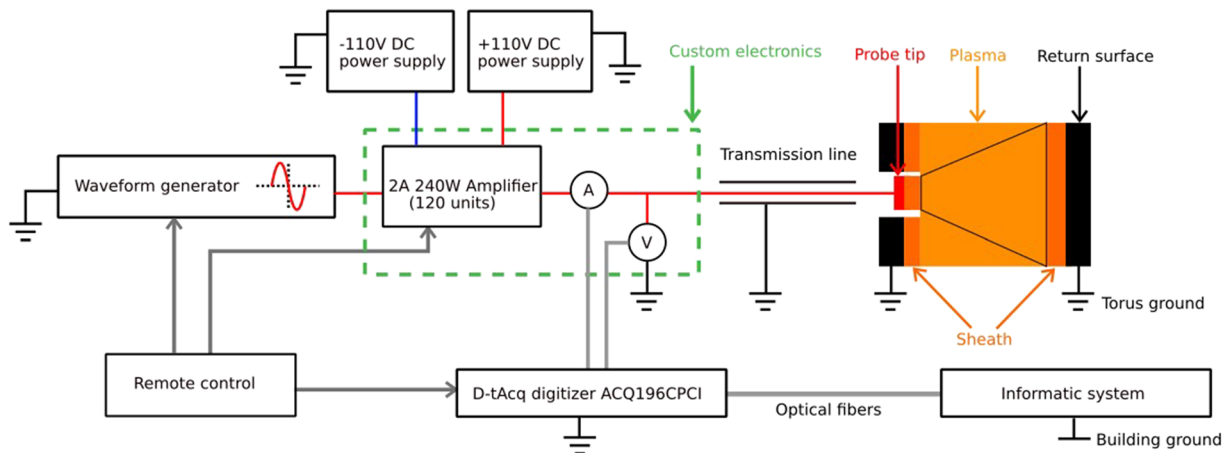


FIG. 6. Diagram including the main components of the electronic system and the equivalent circuit for the Langmuir probe with the current flowing between the probe tip and a larger return surface.

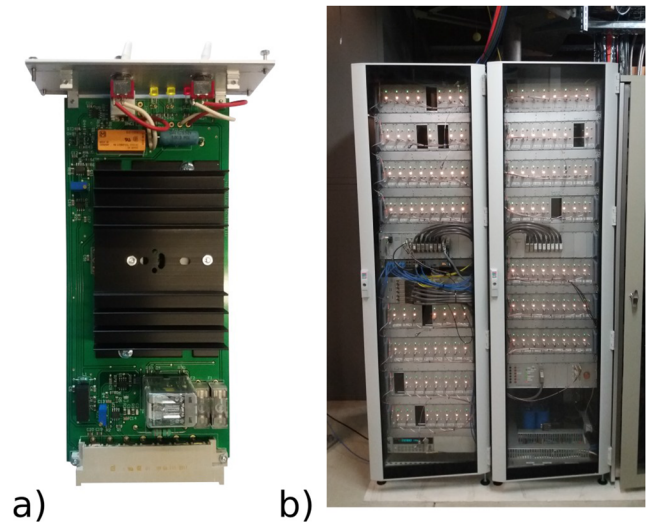


FIG. 5. Single amplifier (a) and complete cubicle (b). Amplifiers have been removed where the in-vessel transmission line has been damaged.

A single amplifier module is shown in Fig. 5, as well as the cubicle installed in the TCV basement level. The organization of the electronics of a single amplifier within the complete diagnostic environment is illustrated schematically in Fig. 6, and a complete drawing of the circuitry is given in Fig. 7.

Amplifiers, waveforms, acquisitions, and power supplies are all referenced to the torus ground. Electrical insulation from the building ground is provided with optical fibers once the signal has been digitized; see Fig. 6.

#### A. Requirements

On TCV, the following relation is assumed for the current flowing through the sheath and to the probe as a function of applied

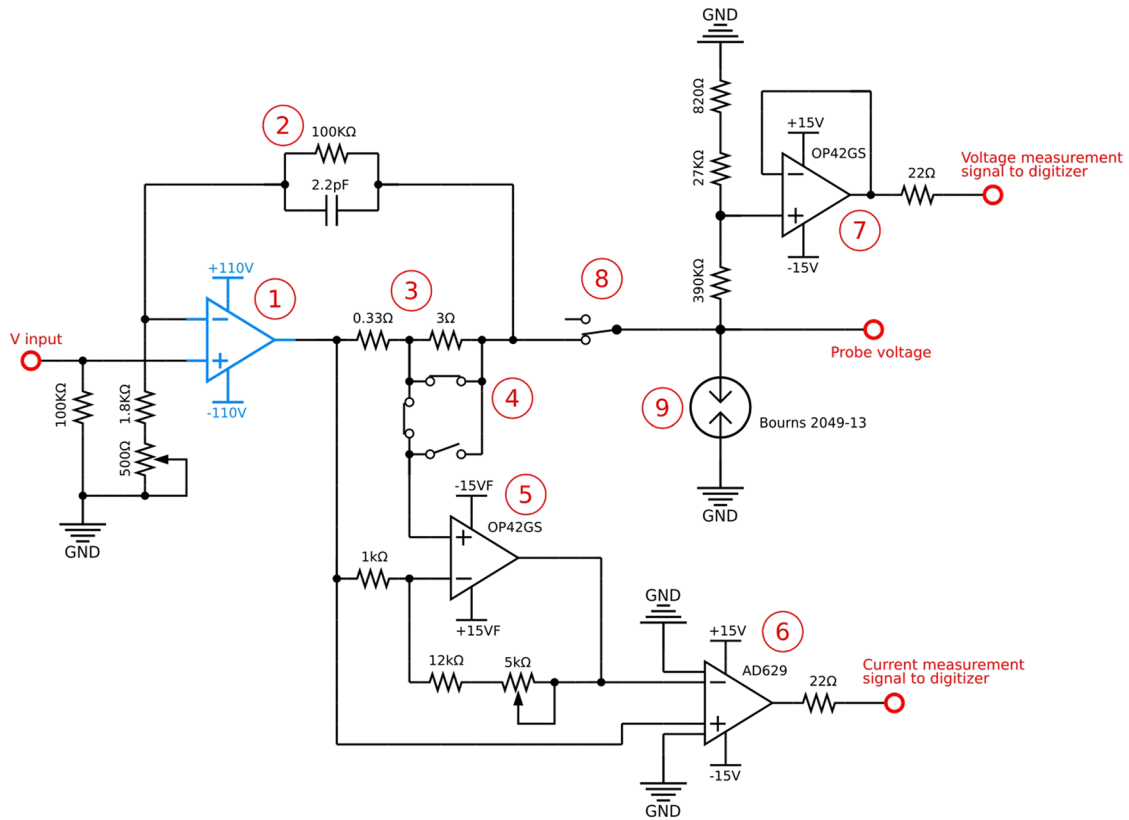


**FIG. 7.** Custom Langmuir probe electronics: ① custom amplifier in blue (see Fig. 8), ② overall negative feedback loop, ③ shunt resistors, ④ shunt relays (here the 3 Ω resistor is bypassed to select the large current measurements ±2 A), ⑤ OP-Amp used to amplify the current measurement signal (the potential drop across the shunt resistors), ⑥ high common mode unity gain OP-Amp referencing to ground the current measurement signal, ⑦ OP-Amp used as a voltage divider for the potential measurement, ⑧ switch to select either the biased probe potential mode  $V_{pr}$  or the floating potential mode  $V_{fl}$ , and ⑨ surge protection.

probe voltage:<sup>6</sup>

$$I_{pr} = I_{sat} \left[ 1 + \alpha(V_{pr} - V_{fl}) - e^{\frac{V_{pr} - V_{fl}}{T_e}} \right], \quad (2)$$

where  $V_{fl}$  is the potential at which there is no net current drawn from the plasma,  $\alpha$  is a coefficient taking into account the increase in the effective ion collection area with voltage in the ion saturation domain due to sheath expansion,  $T_e$  is the electron temperature expressed in electron volts, and  $I_{sat}$  corresponds to the ion current drawn at  $V_{pr} \leq V_{fl}$ . In the case of probe tips with relatively small ion collection area, e.g., flush probes, the parameter  $\alpha$  is mandatory for the interpretation of measurements. It is less critical in the case of domed probes.

The ion saturation current  $I_{sat}$  is given by the Bohm condition,<sup>4</sup>

$$I_{sat} = n_{e,se} e c_s S, \quad (3)$$

where  $n_{e,se}$  is the electron density at the entrance of the sheath,  $S$  is the effective ion collection area of the probe, and  $c_s$  is the Bohm velocity, given by<sup>4</sup>

$$c_s = \sqrt{\frac{e(T_e + \gamma T_i)}{m_i}}, \quad (4)$$

where  $e$  is the elementary charge,  $T_e$  and  $T_i$  are the electron and ion temperature expressed in eV,  $m_i$  is the ion mass, and  $\gamma$  is the adiabatic index.  $\gamma = 1$  is chosen as a default value to assure compatibility with previous TCV studies.<sup>6</sup> It corresponds to the sound speed of an isothermal plasma. Since  $T_i$  is difficult to measure in the boundary plasma of tokamaks, the assumption that  $T_i = T_e$  is usually made.<sup>6</sup>

In order to measure the current-voltage characteristics described in Eq. (2),  $V_{pr}$  must be swept from a strongly negative voltage  $V_- \approx V_{fl} - 3T_e$  to obtain sufficient saturation for the ion flow, up to the plasma potential  $V_p \approx V_{fl} + 3T_e$ .<sup>4</sup>

The floating potential is usually found in between  $V_{fl} = -30$  V and  $V_{fl} = +15$  V in TCV plasmas. Target electron temperatures typically do not exceed  $T_e \approx 30$  eV. Therefore, the biased probe voltage should range at least from  $V_{min} \approx -30$  V -  $3 \times 30$  V = -120 V up to  $V_{max} = 15$  V +  $3 \times 30$  V = 105 V. Two separated DC power supplies have been selected to provide the sufficient extrema voltages  $V_{pr} = \pm 110$  V. It should be noted, however, that for some discharges, the floating potential is extremely low and  $T_e$  is above 30 eV, e.g.,  $V_{fl} = -45$  V and  $T_e = 45$  eV for shot #58182 (low density, high plasma current, high confinement mode discharge). In this particular case, the amplifiers are unable to apply a voltage low enough to fully approach ion saturation.



amplified 50 times with the overall negative feedback loop on the custom amplifier circuitry; see item ② in Fig. 7 and item ② in Fig. 8. The gain is precisely tuned on each amplifier by changing the resistance of the 500  $\Omega$  potentiometer.

A 2.2 nF capacitance has been set on the negative feedback loop of the first OP-Amp; see item ① in Fig. 8. This capacitance primarily determines the measured cutoff frequency of the overall amplifier  $f_{cutoff} \approx 25$  kHz for stability purposes. The cutoff frequency is much higher than the typical sweeping frequency necessary for time-averaged measurements  $f_{sweep} \approx 300$  Hz. However, it does not allow the ultra fast sweeping required to resolve fluctuations from plasma microturbulence.<sup>13</sup>

The second OP-Amp, see item ③ in Fig. 8, is a so-called *suspended OP-amp*: the potential reference  $V_F$  of the positive and negative power supplies  $V_F \pm 15$  V is very close to the probe voltage, therefore suppressing the need for any large potential differences at the OP-Amp terminals.

#### D. Potential and current measurement system

The voltage measurement consists in dividing the probe voltage by a factor of 15 before the analog-to-digital conversion with a resistive divider. The OP-Amp OP42GS, item ⑦ in Fig. 7, is connected as a voltage follower, and the resistances are selected in order to obtain  $\pm 10$  V at the digitizer when the probe voltage is  $\pm 150$  V. The acquisition is provided by D-TACQ Solutions Ltd.<sup>®</sup> ACQ196CPCI 16 bit digitizers sampling at 200 kS/s. The voltage measurement range is sufficient to cover the power supply range  $\pm 110$  V. Probe voltages beyond  $\pm 150$  V are obtained only in the nonstationary case of plasma disruptions with the probes in the  $V_{fl}$  mode.

The current measurement system is more complex than the voltage measurement one. In the first generation of amplifiers, the voltage drop across the shunt resistors was directly sent to the differential inputs of a high common mode unity gain OP-Amp. The voltage drop range is  $\pm 0.66$  V, and it was then amplified to match the digitizer input voltage range  $\pm 10$  V. Virtual currents originating from the imperfect common mode rejection were acquired, as shown in Fig. 9. These residual currents have to be subtracted from the data by averaging the traces before or after the plasma discharge. OP-Amps AD629 have also been used in other Langmuir probe systems in a similar fashion in order to address the issue of common mode rejection.<sup>14</sup>

In the third generation of amplifiers, the potential drop through the shunt resistors is first amplified with an OP-Amp; see item ⑤ in Fig. 7. The signal is then referenced to ground potential through the high common mode unity gain OP-Amp AD629 in order to be acquired; see item ⑥ in Fig. 7. Virtual currents have been highly reduced, thanks to the higher signal to common-mode ratio, as seen in Fig. 9. The subtraction of virtual currents is still maintained in the routines for the Langmuir probe analysis<sup>6</sup> because capacitive currents are still present with the new electronics.

The current measurement is calibrated in order to obtain  $\pm 10$  V at the digitizer when the current is  $\pm 0.2$  A in the low current mode and  $\pm 2$  A in the high current mode. Dense and hot plasma at the probe can regularly attain the 2 A acquisition limit in electron saturation. The saturation of the acquisition does not represent any significant information loss since data points in the electron saturation region are not taken into account by the minimum temperature

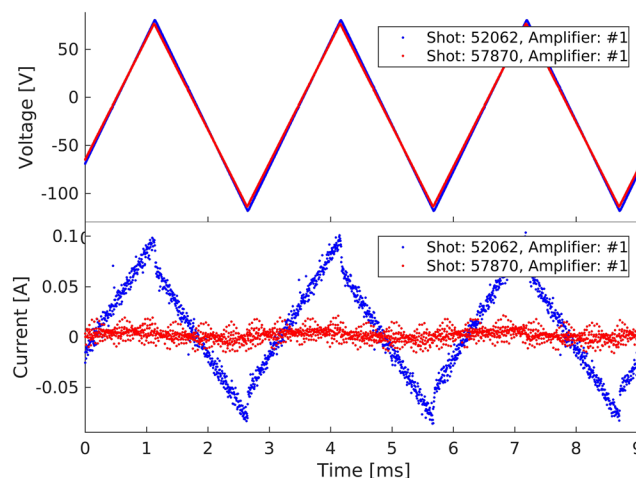


**FIG. 9.** Current measurement during a triangular voltage sweep from the first generation of amplifier in shot #52062 and from the third generation amplifier in shot #57870. Virtual/capacitive current is recorded after the end of the plasma discharge.

method chosen for the 4 parameter fit of the  $IV$  curve<sup>6</sup> given in Eq. (2).

In the case of negative bias and when the shunt selection for large current  $\pm 2$  A is chosen, the current limitation is always above the probe current, which is typically  $I_{sat} < 0.36$  A; see Eq. (5).

The measured resonance frequency point of the current measurement system is  $f_{res} \approx 250$  kHz. Therefore, any current fluctuation faster than the upper cutoff frequency  $f_{cm} \approx f_{res}$  cannot be seen in the acquired data.

#### E. Current limitation system

Current limitation is necessary to avoid overcurrents in the silicon power transistors to limit heat-flux onto the probe tips (in the electron saturation region) and to avoid the current starvation of the high voltage power supplies  $\pm 110$  V which can happen when many probes draw high currents at the same time.

The current limits are determined by the sum of the diode threshold voltages from the transistors BC817 and BC807, see items ⑦ and ⑧ in Fig. 8, and from the 2 diodes 1N4148W. Once the voltage drop across the shunt resistors overcomes the sum of the diode threshold voltages  $V_{threshold} \approx 0.6$  V +  $0.6$  V  $\approx 3.33 \Omega \times 0.35$  A or  $0.33 \Omega \times 3.5$  A, the OP-Amp OPA551UA delivers current directly to the Langmuir probe and the silicon power transistor is bypassed. The large current requested by the overall feedback loop can rapidly damage the OP-Amp OPA551UA. This is why a 270  $\Omega$  resistor has been installed to starve the floating power supply of the OP-Amp OPA551UA once the return current becomes larger than  $I_{max} \approx \frac{15 \text{ V}}{270 \Omega} \approx 55$  mA. Therefore, even though the voltage required by the overall feedback, item ② in Fig. 8, is still very high, the effective voltage at the OP-Amp OPA551UA output and the probe voltage are lower, just enough to supply the current limit  $\pm 0.35$  A/ $\pm 3.5$  A.

Tests of the current limitation system are presented in Fig. 10 for the  $\pm 0.2$  A shunt mode and in Fig. 11 for the 2 A shunt mode.

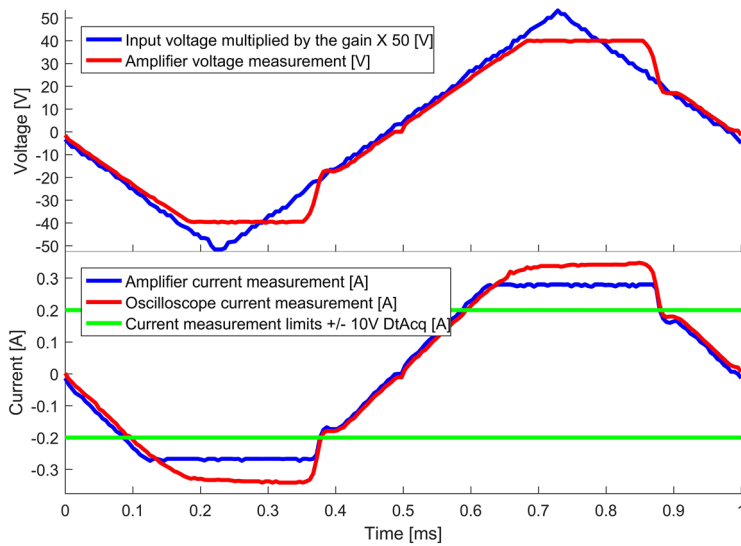


**FIG. 10.** Current limitation test with a 1 kHz triangular voltage sweep, 100  $\Omega$  load, and the shunt selection for small current measurements  $\pm 0.2$  A.

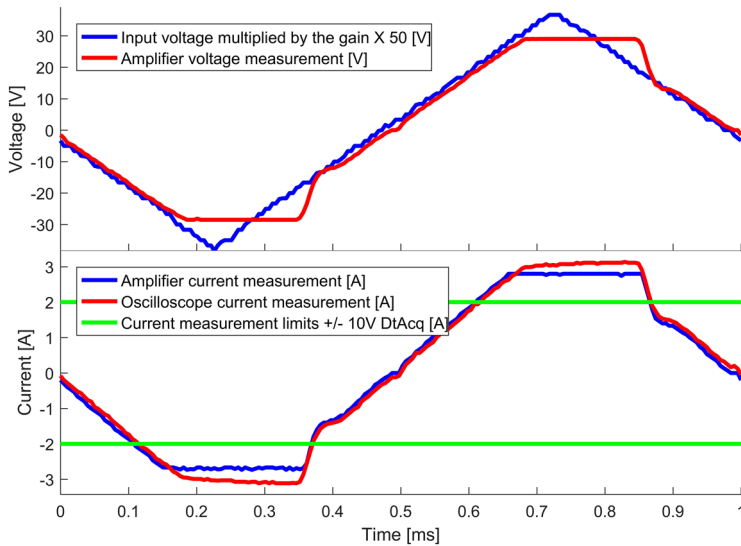


**FIG. 11.** Current limitation test with a 1 kHz triangular voltage sweep, 10  $\Omega$  load, and the shunt selection for large current measurements  $\pm 2$  A.

A specific setup with a voltage isolator device connected to an oscilloscope referenced to ground is required to measure the actual current limit. Indeed, the maximum current measurable by the amplifier circuitry is lower than its actual current limitation  $\approx \pm 0.35$  A/ $\pm 3.5$  A due to the finite voltage  $V_F \pm 15$  V supplying the OP-amp AD629, item ⑥ in Fig. 7. The test frequency  $f = 1000$  Hz is chosen to be similar to the typical sweeping frequency used at TCV. The test peak voltages and the test resistors 10  $\Omega$  and 100  $\Omega$  have been chosen in order to attain the current limit.

The probe current is limited to  $I_{pr} \approx \pm 0.35$  A as shown in Fig. 10 when both shunt resistors are connected. It is limited to  $I_{pr} \approx \pm 3.5$  A when the 3  $\Omega$  shunt resistor is bypassed, as shown in Fig. 11. The  $\pm 0.27$  A and  $\pm 2.7$  A plateaus observed with an oscilloscope for the amplifier current measurement, plotted in blue in the bottom panels of Figs. 10 and 11, correspond to the saturation of the high common

mode OP-Amp due to the finite voltage supply  $\pm 15$  V. The measurement would have been limited to  $\pm 10$  V if the measurement had been done with the digitizers instead of an oscilloscope, as explained in Sec. III D.

#### IV. PROTECTION AGAINST AMPLIFIER DAMAGE

The silicon power transistors, items ⑤ and ⑥ in Fig. 8, are the most frequent components responsible for amplification failure. Usually both components are damaged at the same time. This may lead to a short circuit between the power supply terminals  $\pm 110$  V which is rapidly stopped by 2 A fuses installed in series with the power supply terminals of each amplifier. The transistors for the current limitation, items ⑦ and ⑧ in Fig. 8, are also damaged in  $\approx 20\%$  of the cases. The typical rate of failure is one amplifier per week of

probe operation at TCV with the loss of 29 amplifiers between July 2017 and April 2018.

These failures can be caused by current surges faster than the time response of the current limitation system described in Sec. III E. It can also be caused by absorption of energy when the plasma itself transiently acts as a power supply instead of a load. The power transistors are indeed vulnerable to nonstandard operation such as base-emitter junction breakdown in this case.

These processes mostly occur during transient plasma events such as tokamak plasma current disruptions, Edge Localized Mode (ELM) transients, and electron cyclotron microwave power not absorbed by the plasma. The corresponding time scales of these processes are  $\approx 0.5$  ms and  $\approx 1$  ms (typical durations of the plasma thermal quench and the plasma current quench),  $\approx 0.5$  ms (ELMs), and  $\approx 1$  s (microwave power).

The lack of effectiveness of fuse protection in TCV is discussed in Sec. IV A. An unsuccessful attempt to prevent amplifier damage with overvoltage surge protectors is described in Sec. IV B. The possibility of adding extra inductances to limit fast current peaks is described in Sec. IV C. Finally, another possible solution to avoid amplifier damage by decreasing the effective capacitance of the power supply is described in Sec. IV D.

### A. Attempt to prevent amplifier damage with fuses

Cartridge fuses FSF5X20250V2A (reference 0034.1519) were used in series with the transmission line on the first generation of amplifiers. Due to the inefficiency of these fuses, it was decided to eliminate them in the latest generation.

The lack of fuse effectiveness is believed to be linked to the fuse breaking time. Even if the current is large enough to provide the integrated energy  $RI^2\Delta t$  necessary to melt the conductor, at least a few milliseconds are required for any fuse to completely stop the current<sup>15</sup> due to the formation of an electrical arc. Therefore, the fuse would not protect the transistors during the first  $\Delta t = 1$  ms of any off-normal events, regardless of the current value.

### B. Attempt to prevent amplifier damage with surge protectors

The main purpose of using surge protectors is to prevent the probe potential from exceeding the power supply range  $\pm 110$  V.

Surge protectors, as well as varistors,<sup>16</sup> fulfill protection requirements because of their fast time response (ranging from  $\approx 50$  ns to  $10$   $\mu$ s depending on the product). Surge protectors Bourns<sup>®</sup> 2049–13 with the specified DC sparkover 130 V were connected directly in between the transmission line conductor and ground; see item ⑨ in Fig. 7. Once the voltage difference between the grounded electrode and the electrode at probe voltage is higher than the surge protector breakdown voltage, a Paschen discharge is initiated in the low pressure gas chamber to short-circuit the transmission line. The surge protector breakdown was tested in the laboratory, as described in Sec. IV B 1, and surge protectors were then installed in the machine to evaluate the protection effectiveness, as described in Sec. IV B 2.

#### 1. Testing surge protectors before installation at TCV

A test has been done without any resistive load at the amplifier output in order to see the bare surge protector current. Once the

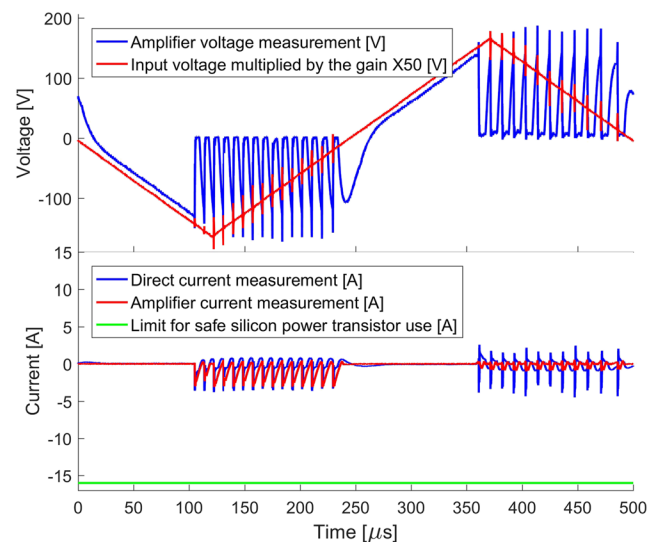


FIG. 12. Time traces of the surge protection being switched on with a triangular waveform at 2 kHz. Each sawtooth oscillation consists of three different phases: the discharge time, a glow period, and the voltage ramp-up time of the amplifier.

surge protector is triggered, current and voltage show a characteristic sawtooth behavior oscillating at  $\approx 100$  kHz, as shown in Fig. 12. The maximum current rating  $I_{collector} = 16$  A according to the manufacturer for the silicon power transistors has been plotted in the same figure. All of the current signals shown in Fig. 12 correspond to the current flowing through the surge protector. The  $\approx 10$   $\mu$ s period of this sawtooth oscillation is the sum of the measured breakdown time  $t_{breakdown} \approx 1$   $\mu$ s, a glow period  $t_{glow} \approx 4$   $\mu$ s, and the voltage ramp up time constant  $t_{ramp} \approx 5$   $\mu$ s. Once triggered, surge protectors switch off again once the voltage applied is reversed. Therefore, it assures reliable data acquisition 0.75 ms after any event that could have triggered the surge protector (1/4 of the typical triangular waveform sweeping period applied).

#### 2. Installation of surge protectors at TCV and unsuccessful protection

The installation of surge protectors on 30 amplifiers out of 114 did not decrease the failure rate. From March 2018 to July 2018, 3 out of the 13 damaged amplifiers were equipped with surge protectors. The surge protectors on the damaged amplifiers did not show any sign of fatigue. For one of these damaged amplifiers, the time traces of the event were recorded in the experiment #60093, as shown in Fig. 13. In this figure, it can be seen that after the disruption, amplifier #103 is no longer able to provide the  $-100$  V voltage required for  $I_{sat}$  measurement, proving that the silicon power transistor lost its semiconductor properties. It is interesting to notice that the time derivatives of the current are very high, sometimes exceeding  $2$  A/5  $\mu$ s (the positive acquisition limit divided by the acquisition period).

The lesson learned is that amplifier failure can happen within the voltage range from the power supplies  $\pm 110$  V, and therefore, surge protectors do not offer an adequate protection.

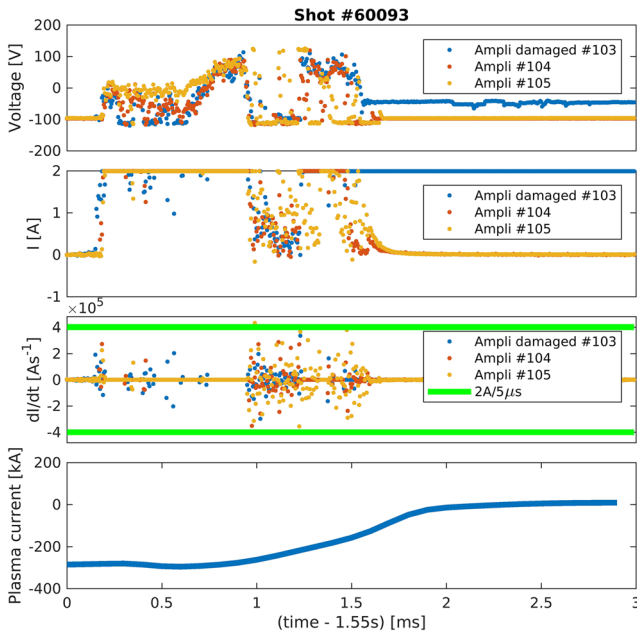


**FIG. 13.** Time traces during a disruption where the amplifier connected to probe #103 is damaged. For comparison, time traces of neighboring amplifiers are also shown.

### C. Preventing amplifier damage by increasing the transmission line inductance

In order to limit the peak current flowing before the current limitation system has time to trigger, a simple solution is to increase the inductance of the transmission line. Any sudden current change would change the probe voltage in order to oppose the increase in current following the equation  $U_L = -Ldi/dt$ . The second positive effect would be to stabilize the emitter and collector voltages of the transistor in order to avoid the emitter voltage to transiently surpass the base voltage.

In Secs. IV C 1–IV C 3, some explanations and calculations are presented in order to describe the protection mechanism and to justify the choice of the proper inductance value required for protection.

#### 1. RLC equivalent circuit and measurement considerations

The transmission line can be modeled as a single RLC circuit because, at the cutoff frequency of the amplifier current

measurement  $f_{cm} \approx 250$  kHz, the wavelength of any fluctuation is much longer than the transmission line length  $\approx 20$  m,

$$\lambda = \frac{c_{Mueller}}{f} = \frac{1}{f_{cm} \sqrt{L_{Mueller} C_{Mueller}}} \approx 350 \text{ m}, \quad (7)$$

where  $c_{Mueller}$  is the speed of light in the 19 pair Mueller cable,  $f_{cm} = 250$  kHz is the cutoff frequency from the amplifier current measurement,  $L_{Mueller} \approx 0.7 \mu\text{H m}^{-1}$  is the inductance per unit length, and  $C_{Mueller} \approx 0.19 \text{ nF m}^{-1}$  is the capacitance per unit length of the 19 pair Mueller cable. The 250 kHz frequency is relevant to consider because most of the plasma fluctuation power was found below  $\approx 250$  kHz at TCV in 2004 with the former fast probe sampling  $I_{sat}$  and  $V_{fl}$  at 6 MHz.<sup>17</sup>

The resistance in the RLC circuit is the sheath resistance  $R_{sheath}(t, V)$ , a function dependent on both time and probe voltage. The equivalent circuit is represented in Fig. 14. The extra inductance should be mounted in series with the transmission line and behind the voltage measurement, in order to take into account the inductive voltage in the measurement of the probe voltage. In any case, inductive voltages can be deduced from the time derivative of current measurements.

#### 2. Determination of the minimum inductance value required

For effective protection, the voltage drop across the inductance should be of the order of a few times  $T_e$ . Current surges above the rating of the silicon power transistors of  $I = 16$  A must be inhibited for the reaction time of  $\approx 5 \mu\text{s}$  of the current limitation system.

Taking a desired voltage drop across the inductance  $U = 100$  V, the required total inductance of the line can be determined,

$$L = \left| -\frac{U}{dI/dt} \right| = \frac{100 \text{ V}}{16 / (5 \cdot 10^{-6}) \text{ As}^{-1}} \approx 31 \mu\text{H}. \quad (8)$$

This value is higher than the inductance of the transmission lines currently installed at TCV,  $L_{line} \approx 15.4 \mu\text{H}$ , and therefore, an additional  $L_{extra} > 15 \mu\text{H}$  would be required. It must be noted that capacitive currents do not play any significant role during large transient events. Indeed, a simple calculation shows that these currents are negligible when compared to the probe current,

$$I_C = C_{line} \frac{dV}{dt} \approx 5 \cdot 10^{-9} \text{ F} \cdot \frac{100 \text{ V}}{5 \cdot 10^{-6} \text{ s}} = 0.1 \text{ A}. \quad (9)$$

#### 3. Determination of the maximum tolerable inductance value

In principle, the extra inductance does not affect the current-voltage measurements because the voltage is measured on the

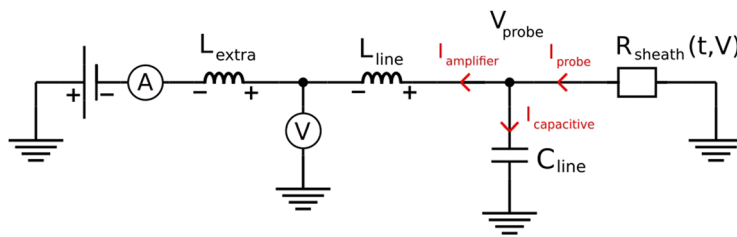


**FIG. 14.** Equivalent RLC circuit for the Langmuir probe taking into account the inductance and the capacitance of the transmission line and an extra inductance. Here,  $I_{amplifier} > 0$  and  $dI_{amplifier}/dt > 0$  were assumed such that the inductive voltages are counteracting the amplifier voltage.

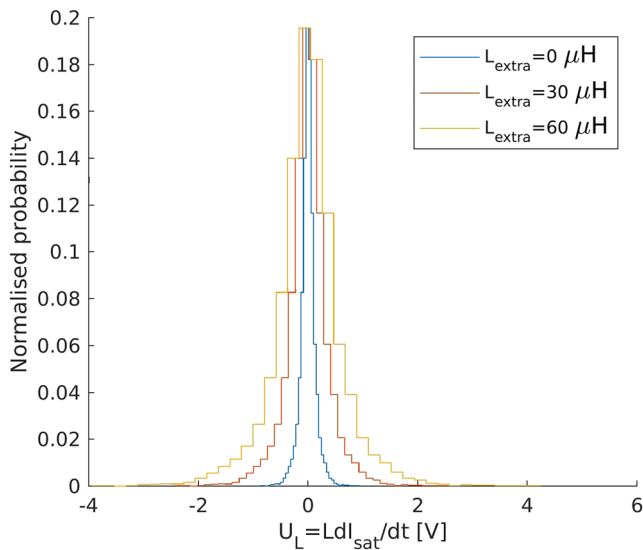


**FIG. 15.** Histograms of calculated inductive voltage in ion saturation ( $V_{pr} < -90$  V) from the standard shot #61273. Three different inductance values are taken for comparison. The data come from probe #6 ( $t = 0.8$  s to  $t = 1.1$  s). This probe was specifically chosen because it was found to have the highest level of fluctuation as compared to other probes.

probe-side of  $L_{extra}$ . The voltage drops between the measurement location and the probe tips across  $L_{line}$  and capacitive currents due to  $C_{line}$  can in principle be corrected for.

However, it is important to ensure that the probe voltage stays well in the ion saturation regime at all times when operating the probes in the  $I_{sat}$  mode (probe current  $I_{pr}$  recorded as a function of time rather than as a function of probe voltage  $V_{pr}$ ). Thus, the probe voltage should not deviate considerably from  $V_{pr} \approx -110$  V at any time. Figure 15 shows the expected inductive voltages for different values of  $L_{extra}$  and for an experimental probe signal with relatively

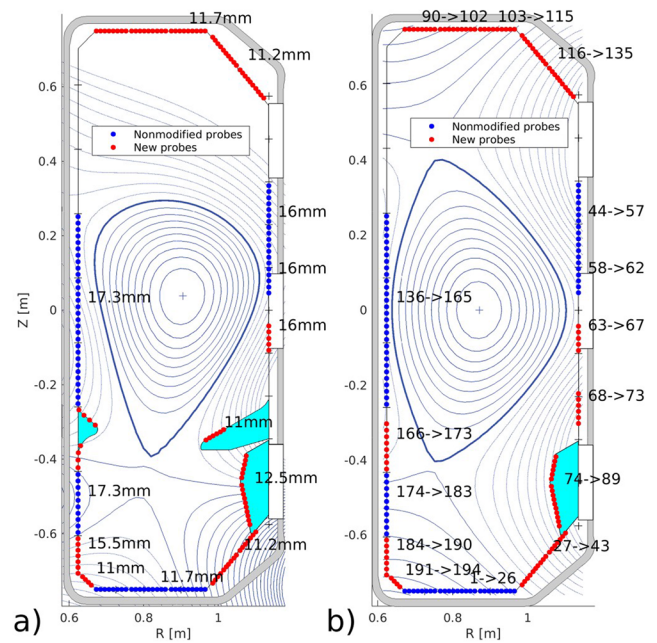


**FIG. 17.** Detail of the Langmuir probe array positions planned for the upgrade. The average distance in between probe tips is displayed for the upgrade with the first version of the baffles<sup>20</sup> to be installed in 2019 in (a) and the probe numbering is shown for the upgrade without baffles in (b).

high current fluctuation levels. This shows that inductive voltages are  $\leq \pm 1$  V ( $< \pm 2$  V) for  $L_{extra} = 30 \mu\text{H}$  ( $L_{extra} = 60 \mu\text{H}$ ) at any time. Therefore,  $L_{extra} = 30 \mu\text{H}$  or even  $L_{extra} = 60 \mu\text{H}$  would be tolerable.

Inductive voltages fluctuating with time will cause capacitive currents. However, the calculated capacitive currents  $I_C = C_{line} \cdot dU_L/dt$  with  $L_{extra} = 30 \mu\text{H}$  are found below 1.5 mA for the same data as in Fig. 15, which is acceptably low when compared to the

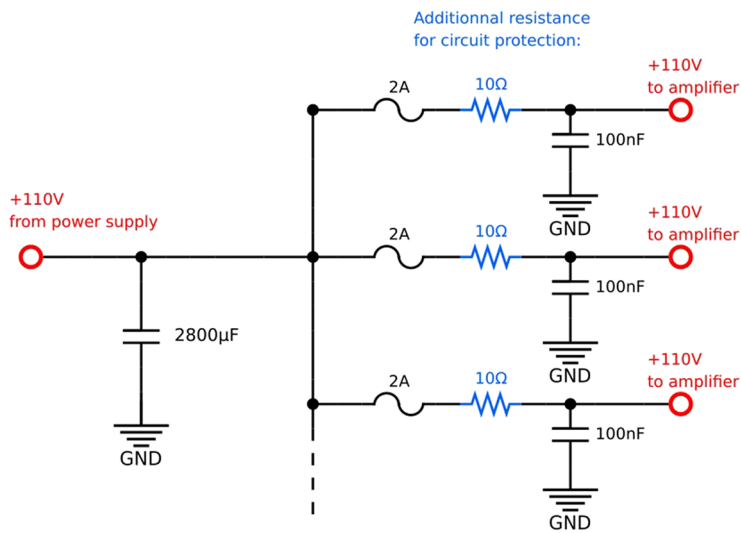


**FIG. 16.** Equivalent circuit for the positive +110 V power supply. All of the 120 amplifiers in cubicles 1 and 2 are connected to the same capacitor. The same circuit applies for the negative  $-110$  V power supply. The additional protective resistances  $R_{extra}$  are highlighted in blue.

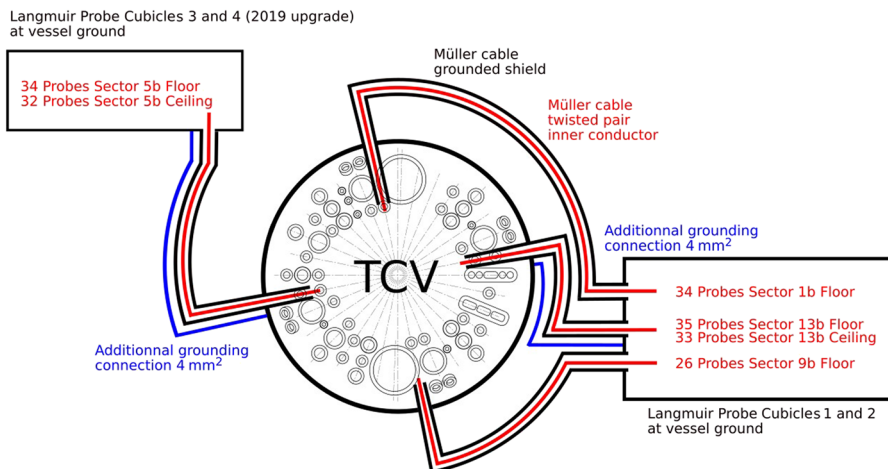


**FIG. 18.** Electrical connections in between the tokamak, the existing and planned electronics cubicles for the divertor upgrade with biased conductors in red, and grounded conductors in black.

time averaged ion saturation current in this experiment  $I_{sat} \approx 0.22$  A. Capacitive currents are expected to be the largest if the  $RLC$  circuit is excited by the time changing sheath resistance at the resonant frequency for  $LC$  circuits,

$$f_{res,LC} = \frac{1}{2\pi\sqrt{L_{line} \cdot C_{line}}} \approx 574 \text{ kHz}, \quad (10)$$

where  $L_{line} = 15.4 \mu\text{H}$  and  $C_{line} = 5 \text{ nF}$ . Increasing the line inductance by adding  $L_{extra} = 30 \mu\text{H}$  would result in lowering the resonant frequency down to  $\approx 336 \text{ kHz}$ . Since most of the plasma fluctuation power has been found below  $\approx 250 \text{ kHz}$ ,<sup>17</sup> the risk of measuring large capacitive currents due to the  $LC$  resonance is relatively low.

To conclude,  $L_{extra} = 30 \mu\text{H}$  could be an appropriate inductance for effective protection against fast current surges ( $< 5 \mu\text{s}$ ) and negligible perturbation to the measurement.

#### D. Preventing amplifier damage by decreasing the effective power supply capacitance

The large capacitor mounted in parallel with the high voltage supply of each amplifier is a disadvantage during plasma transient events because it can provide large amounts of energy to the individual probe tips having the smallest sheath resistances. The issue can be partially solved by adding a resistor in series with the amplifier, see Fig. 16, in order to drop the line voltage in the case of high current excursions.

For instance, in the presence of a 20 A surge during a disruption when the bias voltage is +100 V, the effective sheath resistance is  $R_{sheath} = 100 \text{ V}/20 \text{ A} = 5 \Omega$ . In this case, an additional resistance  $R_{extra} = 10 \Omega$  would lower the current down to  $I = U/R = 100 \text{ V}/(5 \Omega + 10 \Omega) \approx 6.7 \text{ A}$ . This reduction in current would likely be sufficient to prevent transistor damage.

During normal operation, the current can attain 2 A in electron saturation. In this case, the voltage of the power supply would be lowered down to  $V = 110 \text{ V} - R_{extra}I = 110 \text{ V} - 2 \text{ A} \times 10 \Omega = 90 \text{ V}$ . The voltage drop would be acceptable from a physics point of view because most of the voltage ranges in the IV curve would remain accessible.

Circuit safety is always maintained when the voltage command is higher than the power supply voltage at the amplifier. Indeed, the floating power supply voltage  $\pm 15 \text{ V}$  of the second amplification OP-Amp, item ③ in Fig. 8, will drop through the  $270 \Omega$  resistor and therefore limits its current.

The resistance protection solution is thought to be more effective than the inductance protection solution at the time of writing because it could address the problem of current surges regardless of the temporal characteristics. Installation is envisaged on some amplifiers to test the solution.

#### V. FUTURE EXTENDED PROBE COVERAGE

The first step of the ongoing divertor upgrade for the TCV tokamak features the installation of an in-vessel structure to form a divertor chamber and enhanced diagnostic capabilities.<sup>9</sup> New Langmuir probes will be installed to extend the coverage in order to be compatible with alternative divertor configurations<sup>18,19</sup> such as single null with large flux expansion, double null, super-X, and snowflake plasmas. The planned probe coverage in the poloidal plane is shown in Fig. 17 for both baffled and nonbaffled operation. The electrical connection of the new cubicle is located on the other side of the tokamak building; see Fig. 18. Once again, the shield of the transmission lines will be continuous from the cubicles to the vacuum vessel.

#### VI. CONCLUSION AND SUMMARY

This paper has presented the electronics upgrade for the wall-embedded Langmuir probes on the TCV tokamak. The total number of amplifiers has been increased from 48 to 228, which allows all the probes to be operated simultaneously, greatly improving the flexibility of the measurement. The amplifiers are based on an inexpensive circuitry developed at the Swiss Plasma Center.

Details of the new amplifier circuitry have been described, with an emphasis on the amplification system, on the current limitation system, and on the voltage and current measurement system. Different possible solutions have been explored to prevent amplifier damage, which sometimes occurs due to electrical stresses from transient

events during the TCV plasmas. It is concluded that the best solution comprises the addition of an extra resistor between the power supplies and the amplifiers. This solution will be tested in future experimental campaigns. Finally, the future extended Langmuir probe coverage has been introduced, which is one of the many TCV divertor upgrades under development and fabrication and which will substantially improve the diagnostic coverage for a range of magnetic geometries, such as double-null, super-X, and snowflake plasmas.

## ACKNOWLEDGMENTS

This work has been carried out within the framework of the EUROfusion Consortium and has received funding from the Euratom research and training program 2014–2018 and 2019–2020 under Grant Agreement No. 633053. The views and opinions expressed herein do not necessarily reflect those of the European Commission or of the ITER Organization. This work was supported in part by the Swiss National Science Foundation.

## REFERENCES

- <sup>1</sup>F. Hofmann, J. B. Lister, W. Anton, S. Barry, R. Behn, S. Bernel, G. Besson, F. Buhlmann, R. Chavan, M. Corboz, M. J. Dutch, B. P. Duval, D. Fasel, A. Favre, S. Franke, A. Heym, A. Hirt, C. Hollenstein, P. Isoz, B. Joye, X. Llobet, J. C. Magnin, B. Marletaz, P. Marmillod, Y. Martin, J. M. Mayor, J. M. Moret, C. Nieswand, P. J. Paris, A. Perez, Z. A. Pietrzyk, R. A. Pitts, A. Pochelon, R. Rage, O. Sauter, G. Tonetti, M. Q. Tran, F. Troyon, D. J. Ward, and H. Weisen, *Plasma Phys. Controlled Fusion* **36**, B277 (1994).
- <sup>2</sup>S. Coda, J. Ahn, R. Albanese, S. Alberti, E. Alessi, S. Allan, H. Anand, G. Anastassiou, Y. Andrébe, C. Angioni, M. Ariola, M. Bernert, M. Beurskens, W. Bin, P. Blanchard, T. C. Blanken, J. A. Boedo, T. Bolzonella, F. Bouquey, F. H. Braummüller, H. Bufferand, P. Buratti, G. Calabró, Y. Camenen, D. Carnevale, F. Carpanese, F. Causa, R. Cesario, I. T. Chapman, O. Chellai, D. Choi, C. Cianfarani, G. Ciraolo, J. Citrin, S. Costea, F. Crisanti, N. Cruz, A. Czarnecka, J. Decker, G. De Masi, G. De Tommasi, D. Douai, M. Dunne, B. P. Duval, T. Eich, S. Elmore, B. Esposito, M. Faitsch, A. Fasoli, N. Fedorczak, F. Felici, O. Février, O. Ficker, S. Fietz, M. Fontana, L. Frassinetti, I. Furno, S. Galeani, A. Gallo, C. Galperti, S. Garavaglia, I. Garrido, B. Geiger, E. Giovannozzi, M. Gobbin, T. P. Goodman, G. Gorini, M. Gospodarczyk, G. Granucci, J. P. Graves, R. Guirlet, A. Hakola, C. Ham, J. Harrison, J. Hawke, P. Hennequin, B. Hnat, D. Hogeweij, J.-P. Hogge, C. Honoré, C. Hopf, J. Horáček, Z. Huang, V. Igochine, P. Innocente, C. Ionita Schrittwieser, H. Isliker, R. Jacquier, A. Jardin, J. Kamleitner, A. Karpushov, D. L. Keeling, N. Kirneva, M. Kong, M. Koubiti, J. Kovacic, A. Krämer-Flecken, N. Krawczyk, O. Kudlacek, B. Labit, E. Lazzaro, H. B. Le, B. Lipschultz, X. Llobet, B. Lomanowski, V. P. Loschiavo, T. Lunt, P. Maget, E. Maljaars, A. Malygin, M. Maraschek, C. Marini, P. Martin, Y. Martin, S. Mastrostefano, R. Maurizio, M. Mavridis, D. Mazon, R. McAdams, R. McDermott, A. Merle, H. Meyer, F. Militello, I. G. Miron, P. A. Molina Cabrera, J.-M. Moret, A. Moro, D. Moulton, V. Naulin, F. Nespoli, A. H. Nielsen, M. Nocente, R. Nouailletas, S. Nowak, T. Odstrčil, G. Papp, R. Papřok, A. Pau, G. Pautasso, V. Pericoli Ridolfini, P. Piovesan, C. Piron, T. Pisokas, L. Porte, M. Preynas, G. Ramogida, C. Rapson, J. J. Rasmussen, M. Reich, H. Reimerdes, C. Reux, P. Ricci, D. Rittich, F. Riva, T. Robinson, S. Saarelma, F. Saint-Laurent, O. Sauter, R. Scannell, C. Schlatter, B. Schneider, P. Schneider, R. Schrittwieser, F. Sciortino, M. Sertoli, U. Sheikh, B. Sieglin, M. Silva, J. Sinha, C. Sozzi, M. Spolaore, T. Stange, T. Stoltzfus-Dueck, P. Tamain, A. Teplukhina, D. Testa, C. Theiler, A. Thornton, L. Tophøj, M. Q. Tran, C. Tsironis, C. Tsui, A. Uccello, S. Vartanian, G. Verdoolaege, K. Verhaegh, L. Vermare, N. Vianello, W. A. J. Vijvers, L. Vlahos, N. M. T. Vu, N. Walkden, T. Wauters, H. Weisen, M. Wischmeier, P. Zestanakis, M. Zuin, and EUROfusion MST1 Team, *Nucl. Fusion* **57**, 102011 (2017).
- <sup>3</sup>H. M. Mott-Smith and I. Langmuir, *Phys. Rev.* **28**, 727 (1926).
- <sup>4</sup>P. C. Stangeby, *The Plasma Boundary of Magnetic Fusion Devices*, Series in Plasma Physics and Fluid Dynamics (Taylor & Francis, 2000).
- <sup>5</sup>I. H. Hutchinson, *Principles of Plasma Diagnostics* (Cambridge University Press, 2005).
- <sup>6</sup>O. Février, C. Theiler, H. De Oliveira, B. Labit, N. Fedorczak, and A. Baillod, *Rev. Sci. Instrum.* **89**, 053502 (2018).
- <sup>7</sup>C. K. Tsui, J. A. Boedo, P. C. Stangeby, and TCV Team, *Rev. Sci. Instrum.* **89**, 013505 (2018).
- <sup>8</sup>A. Fasoli and TCV Team, *Nucl. Fusion* **55**, 043006 (2015).
- <sup>9</sup>H. Reimerdes, S. Alberti, P. Blanchard, P. Bruzzone, R. Chavan, S. Coda, B. P. Duval, A. Fasoli, B. Labit, B. Lipschultz, T. Lunt, Y. Martin, J. M. Moret, U. Sheikh, B. Sudki, D. Testa, C. Theiler, M. Toussaint, D. Uglietti, N. Vianello, and M. Wischmeier, *Nucl. Mater. Energy* **12**(6), 1106 (2017).
- <sup>10</sup>R. Chavan, R. Pitts, F. Hofmann, C. Hollenstein, J.-M. Moret, R. Rage, and G. Tonetti, in Proceedings of the 17th Symposium on Fusion Technology, Rome, Italy, 14–18 September (North-Holland, 1992), p. 222.
- <sup>11</sup>R. A. Pitts, S. Alberti, P. Blanchard, J. Horacek, H. Reimerdes, and P. C. Stangeby, *Nucl. Fusion* **43**, 1145 (2003).
- <sup>12</sup>R. A. Pitts and P. C. Stangeby, *Plasma Phys. Controlled Fusion* **32**, 1237 (1990).
- <sup>13</sup>B. LaBombard and L. Lyons, *Rev. Sci. Instrum.* **78**, 073501 (2007).
- <sup>14</sup>M. Mitov, A. Bankova, M. Dimitrova, P. Ivanova, K. Tutulkov, N. Djermanova, R. Dejarnac, J. Stöckel, and T. K. Popov, *J. Phys.: Conf. Ser.* **356**, 012008 (2012).
- <sup>15</sup>W. Bussière, *J. Phys. D: Appl. Phys.* **34**, 1007 (2001).
- <sup>16</sup>J. Boedo, G. Gunner, D. Gray, and R. Conn, *Rev. Sci. Instrum.* **72**, 1379 (2001).
- <sup>17</sup>J. Horacek, R. A. Pitts, and J. P. Graves, *Czech J. Phys.* **55**, 271 (2005).
- <sup>18</sup>C. Theiler, B. Lipschultz, J. Harrison, B. Labit, H. Reimerdes, C. Tsui, W. A. J. Vijvers, J. A. Boedo, B. P. Duval, S. Elmore, P. Innocente, U. Kruezi, T. Lunt, R. Maurizio, F. Nespoli, U. Sheikh, A. J. Thornton, S. H. M. van Limpt, K. Verhaegh, N. Vianello, TCV Team, and EUROfusion MST1 Team, *Nucl. Fusion* **57**, 072008 (2017).
- <sup>19</sup>H. Reimerdes, B. P. Duval, J. R. Harrison, B. Labit, B. Lipschultz, T. Lunt, C. Theiler, C. K. Tsui, K. Verhaegh, W. A. J. Vijvers, J. A. Boedo, G. Calabro, F. Crisanti, P. Innocente, R. Maurizio, V. Pericoli, U. Sheikh, M. Spolare, N. Vianello, TCV Team, and EUROfusion MST1 Team, *Nucl. Fusion* **57**, 126007 (2017).
- <sup>20</sup>A. Fasoli *et al.*, in Proceedings of 27th IAEA Fusion Energy Conference, Gandhinagar, India, 22–27 October 2018, paper FIP/P8.